Common-mode Electromagnetic Interference Mitigation for Solid-state Transformers

Dong Jiang[1], *Zhenyu Wang*[1], *Wenjie Chen*[2], *Jianrui Liu*[1], *Xuan Zhao*[1] *and Wei Sun*[1*]

(1. State Key Laboratory of Advanced Electromagnets Engineering and Technology, Huazhong University of Science and Technology, Wuhan 430074, China;
2. School of Electrical Engineering, Xi'an Jiaotong University, Xi'an 710049, China)

Abstract: Solid-state transformers (SSTs) have been widely used in many areas owing to their advantages of high-frequency isolation and high power density. However, high-frequency switching causes severe electromagnetic interference (EMI) problems. Particularly, the common-mode (CM) EMI caused by the switching of the dual active bridge (DAB) converter is conducted through the parasitic capacitances in the high-frequency transformer and impacts the system reliability. With the understanding of the CM EMI model in SSTs, CM EMI mitigation methods have been studied. For passive mitigation, the coupled inductor can be integrated with the phase-shift inductor function to reduce CM EMI. For active mitigation, variations in the DAB switching frequency can help reduce the CM EMI peak. An active EMI filter can also be designed to sample and compensate for CM EMI. Using these methods, CM EMI can be reduced in SSTs.

Keywords: Solid-state transformer (SST), Dual active bridge (DAB), Common-mode, Electromagnetic interference (EMI)

Abbreviation

PWM	Pulse width modulation
EMI	Electromagnetic interference
SST	Solid-state transformer
DM	Differential mode
CM	Common mode
AEF	Active EMI filter
DAB	Dual active bridge
LISN	Line impedance stabilization network
SPS	Single phase shift
EPS	Extended-phase-shift

1 Introduction

Solid-state transformer (SST) technology has emerged in recent decades for various applications, such as in microgrids and transportation electrification [1]. SSTs can be utilized for the interface of different types (AC or DC) of buses with different ratings. In most cases, the core of an SST is a dual active bridge (DAB) converter [2]. The isolation transformer in the DAB has a high frequency owing to the switching of the active bridge converters on the primary and secondary sides, making the isolation transformer much smaller in size than the 50 Hz or 60 Hz transformer. This is the most evident advantage of SSTs. In addition, the active switching control of the power electronic converter can make the interface function flexible and controllable.

The original concept of an SST was proposed a few decades ago; however, without fast and reliable switching power electronic devices, its application has been challenging [1]. In the last two decades, the development of fast switching insulated gate bipolar transistors (IGBTs) and metal-oxide-semiconductor field-effect transistors (MOSFETs), particularly wide bandgap devices, has made the development of SSTs much faster. In microgrids for renewable energy applications and independent power systems in shipboard and traction, SSTs can be used for interfaces at different power levels with flexible control capability [3-4]. Different topologies of active controlled primary and secondary converters can be applied to optimize electromagnetic stress on high-frequency transformers [5].

Manuscript received May 16, 2022; revised July 7, 2022; accepted July 27, 2022. Date of publication September 30, 2022; date of current version August 22, 2022.
* Corresponding Author, E-mail: sunwei198677@hotmail.com
Digital Object Identifier: 10.23919/CJEE.2022.000023

Although SSTs have led to significant progress in power density and control flexibility, the application of active switching power electronics also introduces some new issues over regular line frequency transformers. One of the most serious drawbacks of SSTs compared with conventional transformers is the electromagnetic interference (EMI) caused by high-frequency switching [6-17]. The switching of power electronic devices on either side of the high-frequency transformer introduces high-frequency excitation in the system and generates high-frequency EMI current and radiation. Parasitic parameters in the complex physical system of the SST hardware result in a complex EMI propagation path. EMI couples with the sensitive parts of the SST system and compromises the system reliability. For the source and load, the EMI generated by SSTs is also a serious problem. EMI standards have been developed to regulate the application of power electronic converters on either the source (grid) or the load side.

Common-mode (CM) and differential-mode (DM) EMI can be analyzed using the propagation paths. CM EMI propagates in a unified direction in the main circuit and through parasitic parameters to the ground. Because CM EMI is highly affected by parasitic parameters in the system layout, it is usually more difficult to analyze. In addition, because CM EMI is conducted through the non-ideal part of the components, the negative impact on the system reliability can be more serious.

Since SST is a new technology, the major study area for this converter is with topology, architecture, operation, and control. Although EMI poses a serious issue, studies on EMI in SSTs have been limited in recent years. A preliminary study of EMI mitigation for SSTs was conducted using conventional passive EMI filter components with snubber capacitors, X and Y caps, and a CM choke [6]. A CM EMI model for SSTs should be developed using the parasitic parameters in the system [7] to understand the CM EMI problem.

With more freedom in converter topologies on the SST primary and secondary sides, the active mitigation of EMI is possible. With a three-level active neutral-point-clamped converter on the primary side, the active commutation sequence and system layout can help mitigate the voltage ringing and EMI, particularly the CM current [8-9]. With an optimal shielding design, the EMI in high-frequency SSTs can be reduced [10]. Using the SST high-frequency impedance model, the ringing caused by switching can be analyzed, and the EMI caused by ringing can be mitigated [11].

Using the CM impedance model for the SST system, a CM filter can be designed to reduce the CM current [12]. The CM choke is assumed to be the most effective CM filter for each cell of the SST; however, it brings extra size and weight to the system. Canceling the CM voltage through pulse width modulation (PWM) in each phase is feasible for motor drives [13]. For SSTs, the combination of CM voltage in the phase legs is different, and few prior studies have considered this issue.

The mitigation method on the source side can help reduce the requirement of CM chokes. A typical method is the switching frequency variation, which can help spread the EMI peak to a wider range in the frequency domain [14-18]. Random PWM is a representative method that randomly varies the switching frequency. Consequently, the EMI peak can be reduced. However, for DAB applications, the switching frequency variation should also consider the power fluctuation to ensure that the DC voltage is stable [14]. In addition to random variation, periodic variation can help reduce EMI, along with predictable ripple [16-18]. For AC/DC power conversion, the impact of switching frequency periodic variation has been studied theoretically [17-18]. However, for a DAB or SST, further analysis is required before application.

Another active EMI mitigation method is the active EMI filter (AEF), which uses an active compensation component to cancel the EMI instead of a passive filter [19-21]. The AEF samples and actively compensates for the original EMI noise in the system. Therefore, it can be decoupled from the main power of the converter. Moreover, its size can be relatively small for high-power applications, particularly for CM EMI filters. Applying the AEF to SSTs can also be a feasible solution to reduce the filter size and weight.

In summary, CM EMI mitigation in SSTs is an important but relatively new area of research. The primary approach to CM EMI mitigation can adopt ideas from motor drives and other converters. This

paper discusses a comprehensive study of CM EMI mitigation. Section 2 introduces the modeling of the CM EMI of SSTs as the basis for mitigation. Section 3 presents a coupled inductor as an approach to a passive CM filter. Section 4 discusses active EMI mitigation methods for SSTs, with the variable switching frequency PWM and AEFs as the primary representatives. Finally, Section 5 summarizes the conclusions.

2 Modeling of CM EMI for SSTs

2.1 Description of the DAB and CM EMI problem

Because of its inherent advantages, such as modular symmetrical structure, high power density, galvanic isolation, soft switching, and bidirectional energy transmission, DAB is a common topology for the power transmission stage of SSTs. Fig. 1 shows a circuit schematic of the DAB prototype. The DAB converter consists of primary and secondary full bridges, a high-frequency transformer T (transformer ratio n=1:1 in this study), and a phase-shift inductor L_{ph}.

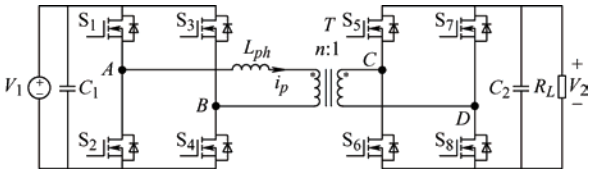

Fig. 1 Circuit schematic of the DAB prototype

It is necessary to clarify the test conditions and derive a detailed high-frequency model of the converter to analyze the CM EMI mechanism in the DAB. Fig. 2 shows the high-frequency DAB model, where a line impedance stabilization network (LISN) is used to measure CM EMI. The LISN was placed between the power supply V_1 and the DAB to examine the influence of interference on power supply network V_1.

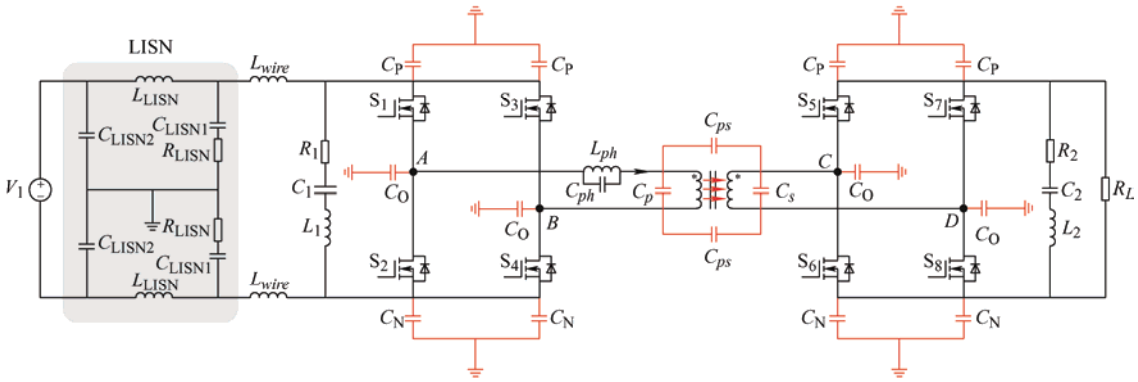

Fig. 2 High-frequency model of the DAB with parasitic parameters

Fig. 2 shows the main parasitic parameters involved in the CM interference path. First, the stray capacitances of the switching modules are the main paths for CM conduction. For example, the power module is a 1.2 kV/300 A SiC power MOSFET module of CAS300M12BM2 from Cree Inc. The stray capacitances C_P, C_N, and C_O of each SiC MOSFET module can be measured using impedance analysis. In addition, the stray capacitances of the high-frequency transformer are the main paths of CM conduction. With a high-power density design, the interwinding capacitance C_{ps} of the transformer is relatively large. It forms a displacement current under the excitation of high dv/dt of the windings, deteriorating CM EMI. In this study, the transformer is equivalent to a lumped model. The stray capacitances can be fitted by testing the open-circuit and short-circuit impedances with an impedance analyzer [22-23]. The complex parasitic parameters and high dv/dt of the DAB result in serious CM EMI problems.

2.2 CM EMI noise separation and calculation

The substitution theorem was applied to derive the CM equivalent model of the DAB. S2, S4, S6, and S8 were replaced with equivalent voltage sources. Capacitors C_1 and C_2 were sufficiently large such that C_1 and C_2 can be regarded as short circuits. Based on the above assumptions, the CM equivalent model of the DAB was obtained, as shown in Fig. 3.

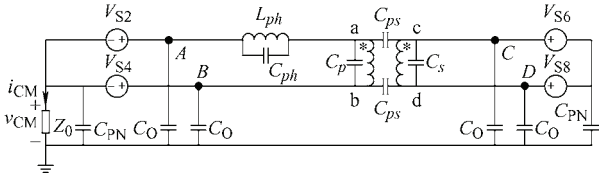

Fig. 3 CM equivalent model of the DAB

$$Z_0 = \frac{Z_{L_{wire}} + \left(Z_{L_{\mathrm{LISN}}} + Z_{C_{\mathrm{LISN2}}}\right) \| \left(R_{\mathrm{LISN}} + Z_{C_{\mathrm{LISN1}}}\right)}{2} \tag{1}$$

$$C_{\mathrm{PN}} = 2C_{\mathrm{P}} + 2C_{\mathrm{N}} \tag{2}$$

Subsequently, the CM noise was analyzed using the superposition theory. The CM and DM voltages of the primary and secondary bridges are defined as V_{CMP} and V_{CMS} and V_{DMP} and V_{DMS}, respectively.

$$\begin{cases} V_{\mathrm{CMP}} = (V_{\mathrm{S2}} + V_{\mathrm{S4}})/2 \\ V_{\mathrm{CMS}} = (V_{\mathrm{S6}} + V_{\mathrm{S8}})/2 \end{cases} \tag{3}$$

$$\begin{cases} V_{\mathrm{DMP}} = (V_{\mathrm{S2}} - V_{\mathrm{S4}})/2 \\ V_{\mathrm{DMS}} = (V_{\mathrm{S6}} - V_{\mathrm{S8}})/2 \end{cases} \tag{4}$$

As shown in Fig. 4, the CM noise generated by the DAB can be decomposed into two parts: the CM noise generated by the DM and CM voltages.

$$\begin{cases} V_{\mathrm{CM}} = V_{\mathrm{CM1}} + V_{\mathrm{CM2}} \\ I_{\mathrm{CM}} = I_{\mathrm{CM1}} + I_{\mathrm{CM2}} \end{cases} \tag{5}$$

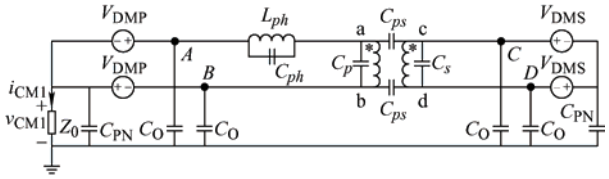

(a) CM EMI generated by the DM voltage

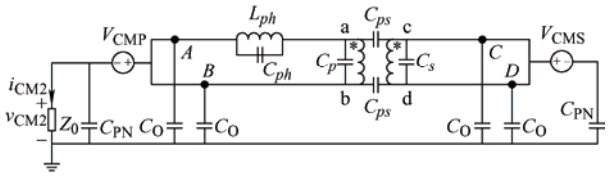

(b) CM EMI generated by the CM voltage

Fig. 4 CM EMI decomposition for the DAB

The EMI model was then simplified, as shown in Fig. 5. First, all the components were paralleled to the voltage sources or through the isolation transformer in parallel with the voltage sources. Subsequently, the transformer with $2\times C_{ps}$ was replaced with a transformer with a ratio of 1:1.

According to Fig. 5a, the CM current generated by the DAB can be derived as follows

$$i_{\mathrm{CM1}} = i_{\mathrm{CM1P}} + i_{\mathrm{CM1S}} \tag{6}$$

$$i_{\mathrm{CM1P}} = \frac{\left(Z_{D2} - Z_{D1}\right)V_{\mathrm{DMP}}}{Z_{D0}Z_{D1} + Z_{D0}Z_{D2} + Z_{D1}Z_{D2}} \frac{Z_{C_{\mathrm{PN}}}}{Z_0 + Z_{C_{\mathrm{PN}}}} \tag{7}$$

$$i_{\mathrm{CM1S}} = \left(\frac{\left(Z_{D5} - Z_{D4}\right)Z_{D3}V_{\mathrm{DMS}}}{\left(Z_{D3}Z_{D4} + Z_{D3}Z_{D5} + Z_{D4}Z_{D5}\right)Z_{D6}} - \frac{V_{\mathrm{DMS}}}{Z_{D6}} \right) \frac{Z_{D7}}{Z_{D7} + Z_0} \tag{8}$$

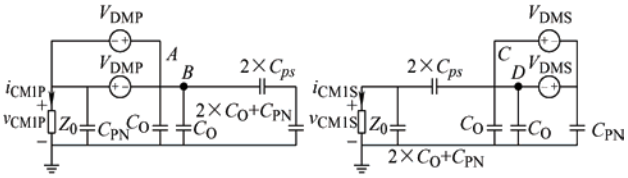

(a) CM EMI generated by the DM voltage

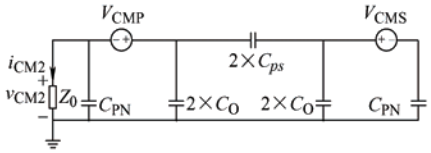

(b) CM EMI generated by the CM voltage

Fig. 5 Simplification analysis of CM EMI

where

$$\begin{cases} Z_{D0} = Z_0 \| Z_{C_{\mathrm{PN}}} \\ Z_{D1} = Z_{C_0} \| \left(Z_{2\times C_{ps}} + Z_{D7}\right) \\ Z_{D2} = Z_{C_0} \\ Z_{D3} = Z_{C_{\mathrm{PN}}} \\ Z_{D4} = Z_{C_0} \| \left(Z_{2\times C_{ps}} + Z_{D7} \| Z_0\right) \\ Z_{D5} = Z_{C_0} \\ Z_{D6} = Z_{2\times C_{ps}} + Z_{D7} \| Z_0 \\ Z_{D7} = Z_{2\times C_0 + C_{\mathrm{PN}}} \end{cases}$$

According to Fig. 5b, the CM current generated by the CM voltages can be derived as

$$i_{\mathrm{CM2}} = \frac{-V_{\mathrm{CMP}}}{Z_{C1}} \frac{Z_{C_{\mathrm{PN}}}}{Z_0 + Z_{C_{\mathrm{PN}}}} + \frac{Z_{C2}V_{\mathrm{CMS}} - Z_{C_{\mathrm{PN}}}V_{\mathrm{CMS}}}{Z_{C2}Z_{C3}} \frac{Z_{C4}}{Z_{C4} + Z_0} \tag{9}$$

where

$$\begin{cases} Z_{C1} = Z_0 \| Z_{C_{\mathrm{PN}}} + Z_{2\times C_0} \| \left(Z_{2\times C_{ps}} + Z_{C4}\right) \\ Z_{C2} = Z_{C_{\mathrm{PN}}} + Z_{2\times C_0} \| Z_{C3} \\ Z_{C3} = Z_{2\times C_{ps}} + Z_{C4} \| Z_0 \\ Z_{C4} = Z_{2\times C_0 + C_{\mathrm{PN}}} \end{cases}.$$

Fig. 6 shows the ideal voltage waveform of the DAB for single-phase-shift (SPS) modulation.

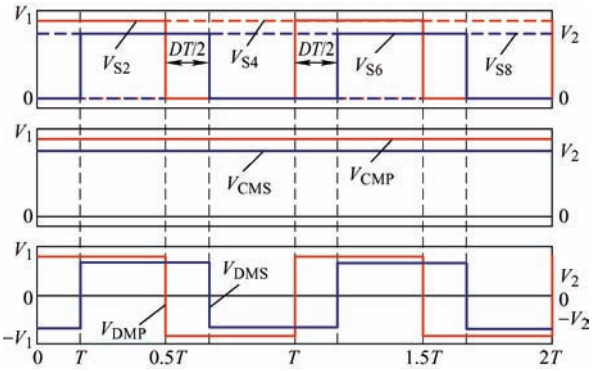

Fig. 6 Ideal voltage of the DAB with SPS modulation

The output voltages of the bridge arms were square waves with a 50% duty cycle. The output voltage V_2 can be derived as

$$V_2 = \frac{(1-D)DV_1TR_L}{2L_{ph}} \tag{10}$$

The CM voltages V_{CMP} and V_{CMS} remain constant, regardless of the nonlinear characteristics of the switching device and the influence of the dead zone. By contrast, the DM voltages V_{DMP} and V_{DMS} are square waves with a 50% duty cycle. Consequently, the CM noise of the DAB is primarily caused by the DM voltages V_{DMP} and V_{DMS} with SPS. Furthermore, CM EMI was introduced owing to the asymmetry of the DAB circuit.

3 Passive CM filter by coupled inductor

Using passive components (filters) to impede the propagation of EMI is a routine solution to EMI mitigation. Integrating an EMI filter with an existing component is a new method to increase the power density. This section introduces passive CM filter integration with a phase-shift inductor in the DAB.

3.1 CM filter by discrete symmetrical inductors

To mitigate the CM noise caused by the DM voltages of the bridges without changing the power transmission characteristics, the phase-shifted inductor was split into two equal halves; these symmetrical inductors were connected in series with each rail of the transformer, as shown in Fig. 7. To prevent magnetic saturation, two discrete inductors were made of a sendust toroid with low permeability, as shown in Fig. 8. Tab. 1 lists the parameters of the discrete inductor.

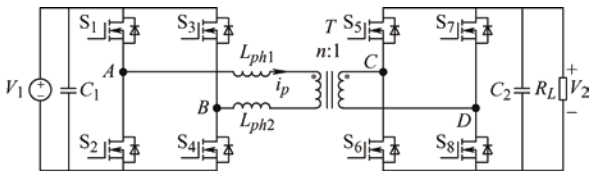

Fig. 7 DAB with uncoupled symmetrical inductors

Fig. 8 Two discrete symmetrical inductors

Tab. 1 Parameters of discrete inductor

Parameter	Value
Inductance/μH	204
Magnetic permeability	26 μ_0
Effective cross-sectional area/cm^2	1.44
Effective mean path length/cm	14.3
Number of turns	78

With discrete symmetrical inductors, the CM EMI decomposition circuits was derived, as shown in Fig. 9. Owing to the symmetrical circuit structure, the primary and secondary DM voltages only form a circulating current through the transformer network, and no CM current is generated. The primary source of CM EMI is the CM voltage of the bridge. Therefore, the CM current is significantly suppressed by SPS.

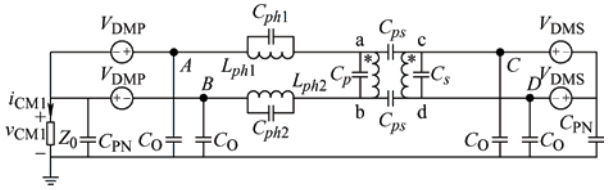

(a) CM EMI generated by the DM voltage

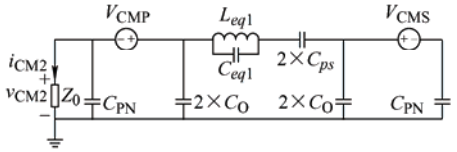

(b) CM EMI generated by the CM voltage

Fig. 9 CM EMI decomposition circuits with discrete symmetrical inductors

As shown in Fig. 5, with the traditional phase-shift inductor structure, the phase-shift inductor is bypassed, and the entire propagation path is capacitive. However, if the phase-shift inductor is split into two discrete inductors, a large equivalent inductance L_{eq1}≈100 μH is introduced into the propagation path, as shown in Fig. 9b, aggravating the CM EMI problem.

Fig. 10 shows the CM impedance spectra of the phase-shift inductor and transformer. When the traditional phase-shift inductor structure was used, the resonant frequency of the transformer and phase-shift inductor was relatively high (9.15 MHz), determined by the leakage inductance and parasitic capacitance C_{ps} of the transformer itself. When symmetrical inductors were used, the resonance frequency was significantly reduced to 706 kHz. The CM voltage of the bridge arms excites a large CM current near the

resonant frequency.

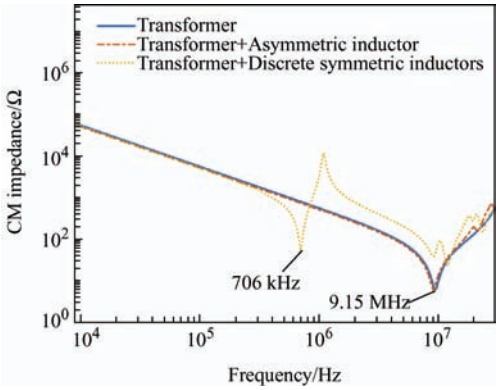

Fig. 10 CM impedance spectrum of the phase-shift inductor and transformer

3.2 CM filter by coupled symmetrical inductor

The uncoupled symmetrical inductors suppress the CM current caused by the DM voltages of the bridge arms; however, they introduce low-frequency resonance, increasing the CM current caused by the CM voltages. To solve this problem, a coupled symmetrical inductor was used to mitigate the CM current, as shown in Fig. 11. Using the coupled symmetrical inductor, the CM EMI decomposition circuits was derived, as shown in Fig. 12.

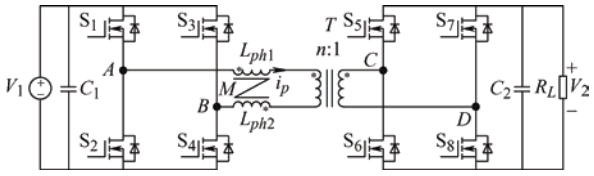

Fig. 11 DAB with coupled symmetrical inductor

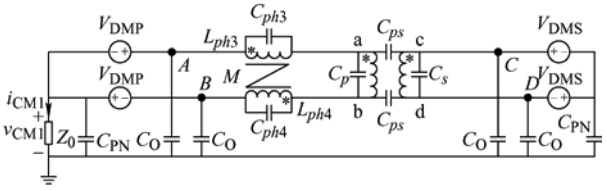

(a) CM EMI generated by the DM voltage

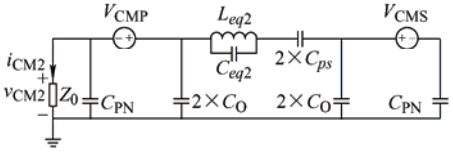

(b) CM EMI generated by the CM voltage

Fig. 12 CM EMI decomposition circuits with coupled symmetrical inductors

Compared with that of discrete symmetrical inductors, the propagation path of the coupled inductors remains symmetrical, suppressing the CM current introduced by the DM voltages of the bridge arms. However, the equivalent inductance L_{eq2} of the coupled inductor is significantly smaller than that of the discrete inductors, which exhibits a better mitigation effect. In this study, the coupled inductor was made of the same material as that of the discrete inductors.

The equivalent inductance L_{eq2} of the coupled inductor is the leakage inductance, which is significantly affected by winding distribution. This study compares the equivalent inductances and CM current reductions of the two winding structures. The two coupled inductor structures are shown in Fig. 13. L_{c1} is a common CM inductor winding structure. The two windings are wound symmetrically along the magnetic core. In L_{c2}, the two banks of the windings are wound evenly along the entire magnetic core. Tab. 2 lists the parameters of the coupled inductors.

Fig. 13 Two coupled inductors with different winding structure

Tab. 2 Parameters of the coupled inductor

Parameter	Values of L_{c1}	Values of L_{c2}
Total inductance/μH	410	407
Leakage inductance/μH	21.6	0.25
Self-inductance/μH	124	102
Mutual-inductance/μH	81	101.5
Magnetic permeability	26 μ_0	26 μ_0
Effective cross-sectional area/cm^2	2.88	2.88
Effective mean path length/cm	14.3	14.3
Number of turns	49+49	39+39

Fig. 14 shows the CM impedance spectra of different inductors and transformers.

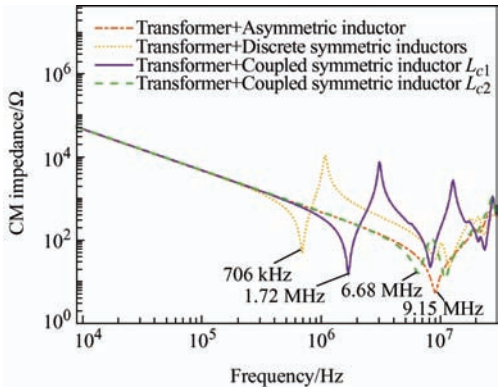

Fig. 14 CM impedance spectrum of different inductors and the transformer

Compared with that of the discrete inductor, the equivalent CM inductance of the coupled inductor was significantly reduced. Consequently, the resonant frequencies of the coupled inductors and transformer increased, particularly that of the coupled inductor L_{c2} (6.68 MHz). This can reduce the CM EMI spikes at low frequencies.

3.3 Experiment verification

To validate the proposed CM filter using a coupled symmetrical inductor, experiments were performed with an experimental platform, as shown in Fig. 15. Tab. 3 lists the main system parameters. The DAB adopted SPS modulation, and the voltage conversion ratio was set to 1 to realize soft switching. In the next few parts, the experiments for active CM EMI mitigation methods were also performed using the same hardware testbed as that for the DAB.

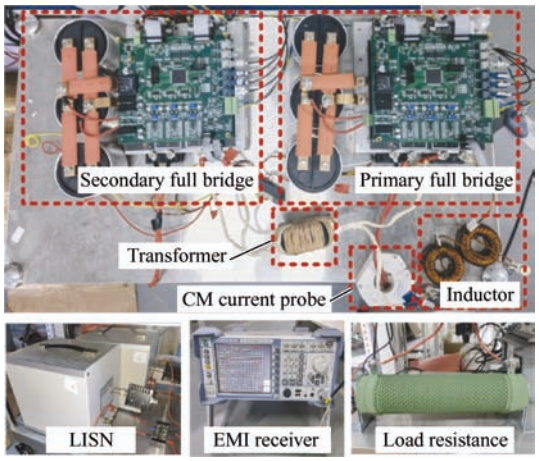

Fig. 15 Experimental platform of the DAB

Tab. 3 Main system parameters of the DAB

Parameter	Value
Switching frequency/kHz	10
Transformer ratio	1:1
V_1/V	150
V_2/V	150
R_L/Ω	30

Fig. 16 show an experimental comparison of CM current with different inductance structures in time domain. The CM current problem of traditional DAB is caused by the asymmetry of phase-shift inductor. As shown in Fig. 16, high-frequency spikes of CM current can be effectively attenuated with all three symmetrical inductors. Furthermore, the CM current in region 1 were almost eliminated.

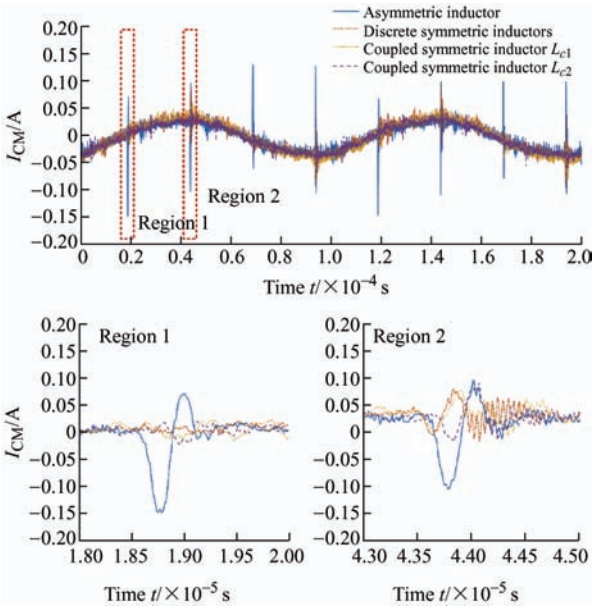

Fig. 16 Experimental comparison of CM current with different inductance structures in time domain

All three symmetrical inductor structures can effectively suppress CM current spikes in the time domain. However, the discrete inductor structure introduces a large equivalent inductance L_{eq} into the CM circuit, worsening the CM EMI at the resonance frequency. Fig. 17 shows an experimental comparison of CM EMI between the asymmetric and discrete symmetric inductors. Discrete inductors effectively attenuated low-frequency (9 kHz-1 MHz) EMI peaks. There was a CM reduction effect of approximately 20 dB at low frequencies. Owing to the resonance problem of the CM impedance, the CM current introduced by the CM voltages of the bridges increased instead; thus, the suppression effect was poor near 700 kHz.

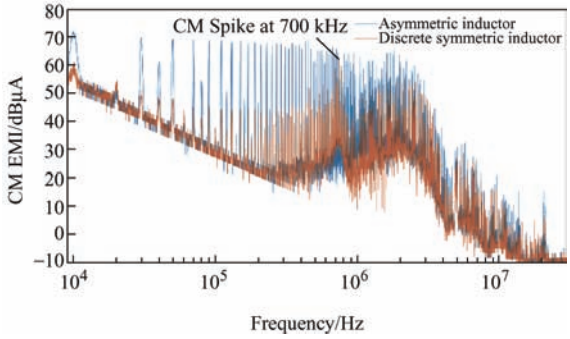

Fig. 17 Experimental comparison of CM EMI between asymmetric inductor and discrete symmetric inductors

To solve this resonance problem, a CM filter using a coupled symmetrical inductor is proposed. Fig. 18

shows an experimental comparison of the CM EMI between the asymmetric and coupled symmetric inductors. The equivalent impedance of the coupled inductor was much smaller than that of the discrete inductors. Moreover, the resonance frequency was greater than 700 kHz; therefore, the CM EMI spike at 700 kHz was effectively improved. Furthermore, compared with L_{c1}, L_{c2} had better high-frequency characteristics with a higher frequency of CM EMI spikes, owing to the smaller leakage inductance. However, in the high-frequency range (1-30 MHz), the CM current was primarily generated by the bridge CM voltage excitation owing to the attenuation of the bridge DM voltages and low CM impedance of the propagation path; therefore, the mitigation effect of the CM filter by the coupled symmetrical inductor is limited.

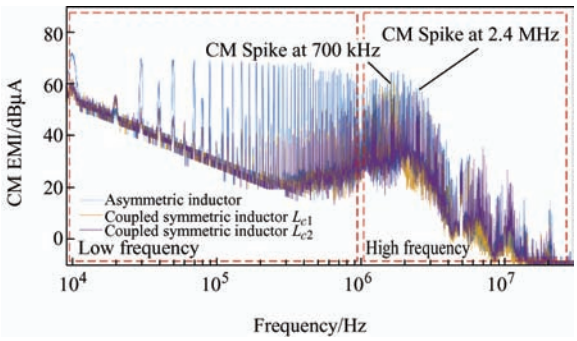

Fig. 18 Experimental comparison of CM EMI between asymmetric and coupled symmetric inductors

In general, the CM filter using the coupled inductor can effectively reduce the CM EMI in the low-frequency band and reduce the volume of the additional EMI filter without affecting the power transmission characteristics.

4 Active CM EMI mitigation

Using passive components can impede CM EMI propagation and introduce more weight. In addition to passive CM filter integration, another approach for CM EMI mitigation in the DAB is to actively shape the CM EMI source. This approach includes a variable switching frequency and active EMI filter.

4.1 Variable switching frequency

Variable switching frequency (VSF) modulation is a typical type of spread-spectrum modulation. By changing the degrees of freedom of the switching frequency, VSF modulation disperses the energy of narrow-band harmonics, originally concentrated in the switching frequency and its multiples to a wider spectrum range, such that the harmonic spikes are attenuated and smoothed. The ability of the VSF modulation to suppress EMI is related to the variation characteristics of the switching frequency. Theoretically, the more evenly the switching frequency is dispersed within the allowable range, the better is the EMI suppression effect. The VSF modulation method with uniform distribution (UD) characteristics was first applied to a three-phase inverter system [17]. In this section, the UDVSF phase-shift modulation applied to the DAB is introduced.

The designed UDVSF modulation exhibits the characteristics of periodic variation; the variation period is assumed to be $T_m=1/f_m$. The switching frequency f_s is defined as a function of θ, where $\theta=2\pi f_m t=\omega_m t$. $D[f_s(\theta)]$ is the distribution density corresponding to the switching frequency function $f_s(\theta)$. The larger the value of $D[f_s(\theta)]$, the greater the distribution of the corresponding switching frequency. According to the analysis of the UDPWM [17], the switching frequency $f_s(\theta)$ and the rate of switching frequency change $|f_s'(\theta)|$ collectively affect the distribution characteristics of the switching frequency.

When the switching frequency changes linearly, a higher switching frequency results in more sampling points and larger $D[f_s(\theta)]$. That is

$$D\left[f_s(\theta)\right] \propto f_s(\theta) \tag{11}$$

For a specific switching frequency, the faster the switching frequency changes, the smaller the number of samples and the smaller the $D[f_s(\theta)]$. That is

$$D\left[f_s(\theta)\right] \propto \frac{1}{\left|f_s'(\theta)\right|} \tag{12}$$

Therefore, the relationship among $f_s(\theta)$, $|f_s'(\theta)|$ and $D[f_s(\theta)]$ satisfies Eq. (13), where k is a scale factor

$$k \cdot \frac{f_s(\theta)}{\left|f_s'(\theta)\right|} = D\left[f_s(\theta)\right] \tag{13}$$

Eq. (13) is a first-order differential equation that requires two boundary conditions to determine the integral constant and scale factor. Boundary conditions can be set according to the periodicity of the switching frequency, as shown in Eq. (14), where f_{upper} is the

upper limit, and f_{lower} is the lower limit of $f_s(\theta)$.

$$\begin{cases} f_s(0) = f_{upper} \\ f_s(\pi) = f_{lower} \end{cases} \tag{14}$$

The distribution density function D [$f_s(\theta)$] of the UDVSF satisfies Eq. (15), which is constant. Therefore, the derivation of Eq. (13) can be used to further obtain Eq. (16).

$$D\left[f_s(\theta)\right] = \frac{1}{f_{upper} - f_{lower}} \tag{15}$$

$$f_s''(\theta) f_s(\theta) - \left(f_s'(\theta)\right)^2 = 0 \tag{16}$$

Combined with Eq. (16) and the boundary condition in Eq. (14), the analytical formula for the switching frequency function $f_s(\theta)$ can be solved as follows

$$f_s = \begin{cases} \exp(A\omega_m t + B) & 0 \leqslant \theta < \pi \\ \exp(A(2\pi - \omega_m t) + B) & \pi \leqslant \theta \leqslant 2\pi \end{cases} \tag{17}$$

where $A = \frac{1}{\pi}\ln\left(\frac{f_{lower}}{f_{upper}}\right)$, $B = \ln\left(f_{upper}\right)$.

Fig. 19 presents the switching frequency waveform of the UDVSF when f_m was 100 Hz, f_{lower} was 10 kHz, and f_{upper} was 20 kHz. Fig. 20 shows the statistical distribution characteristics of the switching frequency; the switching frequency range is equidistantly distributed in ten intervals, and the sampling points of each interval are approximately 10%. The statistical distribution characteristics shown in Fig. 20 prove that the analytical function switching function in Eq. (17) can satisfy the requirements of a UD.

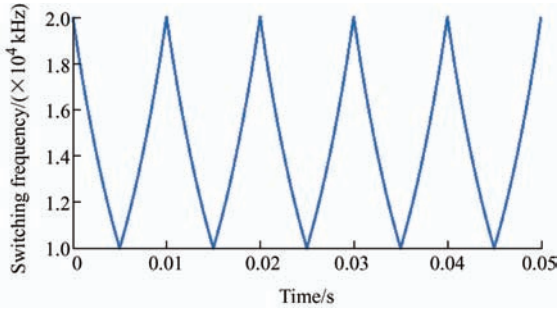

Fig. 19 Switching frequency waveform of UD modulation

Based on the above principle, the variation mode of the switching frequency based on UD was designed. The designed UD method can be directly applied in practice. However, in contrast to AC/DC or DC/AC power conversion, the switching frequency variation may cause fluctuations in the power delivery of the DAB. For general DC/AC converters, the fundamental wave of low frequency (such as 50 Hz) undertakes the main task of power transmission. The high-frequency components of the switching and multiple switching frequencies are typically harmonics that need to be limited. However, for the DAB converter, bidirectional power flow is realized by high-frequency voltage/current through a high-frequency isolation transformer. Therefore, the switching frequency variation may affect power transmission.

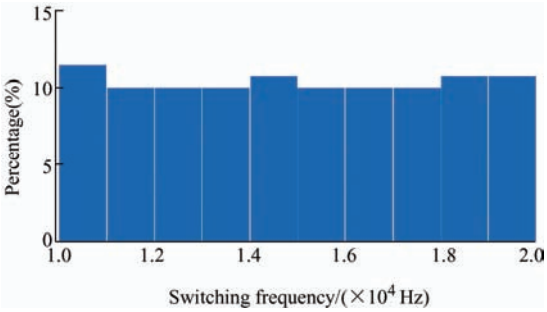

Fig. 20 Statistical distribution of switching frequency

A DAB typically adopts phase-shift modulation methods, such as SPS and extended-phase-shift (EPS), rather than PWM. Taking SPS modulation as an example, the average transmission power of the DAB under SPS modulation can be represented by Eq. (18), where V_1 is the primary-side DC voltage, V_2 is the secondary-side DC voltage, n is the transformer ratio, and D is the phase-shift ratio.

$$P = \frac{nV_1V_2}{2f_sL}D(1-D) \tag{18}$$

The DAB power is inversely proportional to the switching frequency f_s, as shown in Eq. (18). Similarly, other phase-shifting modulation methods are directly related to the switching frequency.

To solve the problem of power fluctuation, it is necessary to control the phase-shift angle (or D) while the switching frequency changes to stabilize the power transmission. A convenient method is to deduce D using Eq. (18); D changes with the switching frequency f_s in each switching cycle.

To validate the proposed UD phase-shift modulation

methods, experiments were performed with an experimental platform. Tab. 4 lists the system parameters. The DAB operates at a constant switching frequency (CSF) modulation with a nominal switching frequency (f_{sN}) used as a reference.

Tab. 4 Parameters of the DAB system with VSF

Parameter	Value
Primary voltage V_1/V	200
Secondary voltage V_2/V	80
Nominal switching frequency f_{sN}/kHz	20
Switching frequency f_{lower}-f_{upper}/kHz	10-20

Fig. 21 shows the experimental results for the primary inductance voltage, primary inductance current, and secondary voltage for the CSF and VSF cases. During the CSF modulation, in addition to the DC component, the secondary-side voltage also contains high-frequency components with a peak value of approximately 0.2 V; however, the content of these high-frequency components is minimal. Therefore, the secondary voltage and power transmission are stable. In the VSF modulation, there is a low-frequency component of 100 Hz with a peak value of approximately 0.3 V, introduced by the periodic variation of the switching frequency. However, after the phase-shift control of each switching cycle, its content is also controlled within a very small range (4‰).

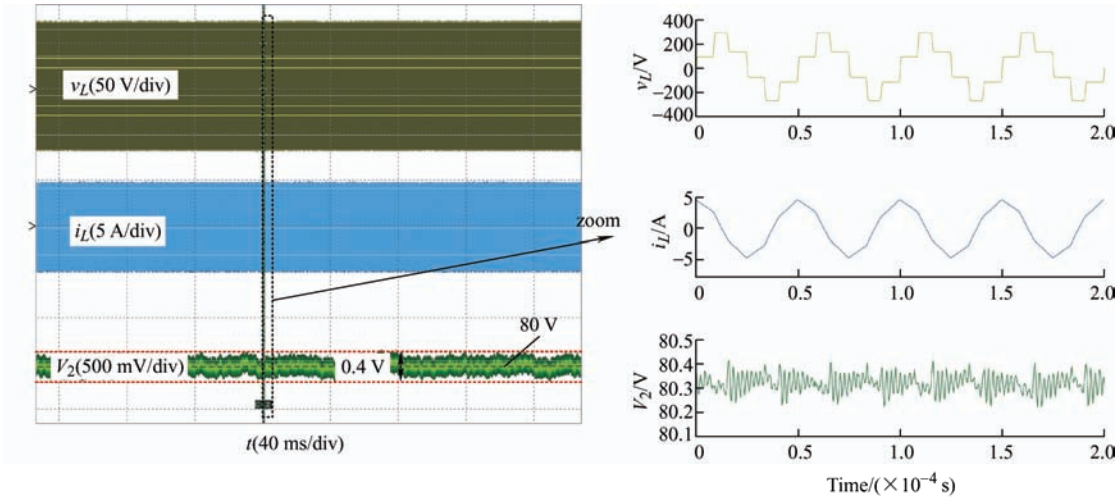

(a) DAB with CSF SPS modulation

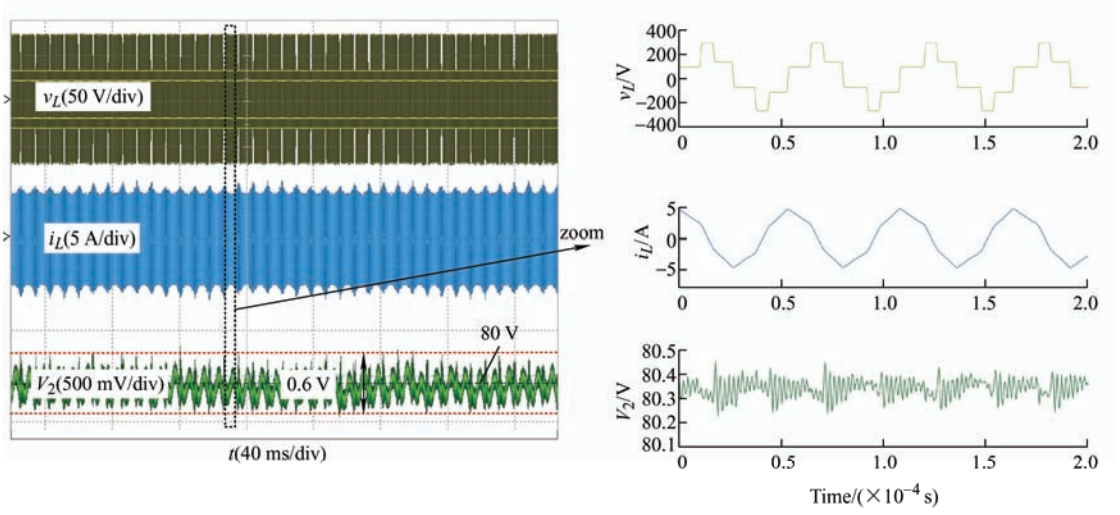

(b) DAB with UD-SPS modulation

Fig. 21 Experimental results of primary inductance voltage v_L, primary inductance current i_L, and secondary voltage V_2

Fig. 22 shows a CM EMI comparison obtained using the EMI test receiver. The application of UD phase-shift modulation in the DAB mitigates CM EMI by up to 10 dB in the frequency range of 150 kHz- 1 MHz, compared with the CSF modulation. In the higher range of 1-30 MHz, the EMI characteristics are dominated by the transient state of the switching action, rather than the PWM; therefore, the CM EMI of the two cases are similar.

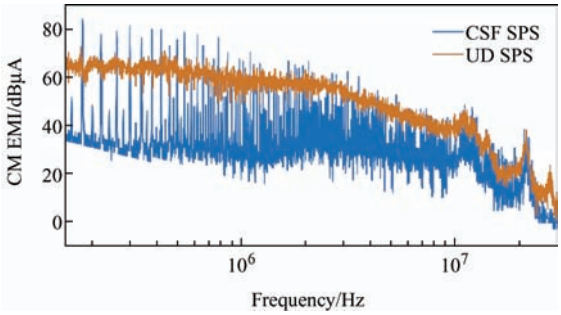

Fig. 22 Experimental comparison of CM EMI

4.2 Active EMI filter

In contrast to the VSF modulation, which shapes the EMI source by PWM, the AEF compensates for the EMI with extra active components. It is primarily composed of three parts: the sensing, amplifying, and compensating sections. The sensing and compensating signals are in the form of voltage or current. Based on the signal types of the sensing and compensating sections, the AEF can be divided into four topologies. In an SST hardware, substantial CM EMI is generated by the high-frequency switching of power electronics and numerous parasitic parameters. To reduce the influence of CM EMI on the power supply and other front-side equipment, this study adopts a current-sensing current-compensating (CSCC)-type of AEF. As discussed in Section 2, there are several ways for CM current to circulate. The CSCC AEF can easily detect the CM current on the DC bus, and the reverse compensating current can be generated and injected into the DC side to eliminate CM EMI directly. Fig. 23 shows a schematic of the feedforward CSCC AEF. $V_{CM}(s)$ represents the equivalent CM voltage. $Z_{CM}(s)$ represents the CM impedance of the testing equipment. $Z_{LISNs}(s)$ represents the impedance of the LISNs. $I_{cancel}(s)$ represents the compensating current generated by the AEF. $A(s)$ represents the entire current amplification of the AEF.

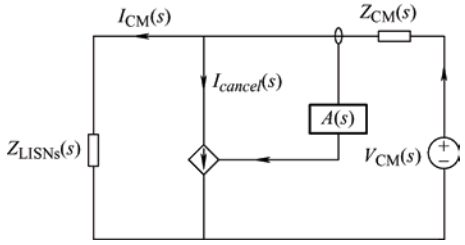

Fig. 23 Schematic diagram of the proposed AEF

With the compensating current $I_{cancel}(s)$ injected, the CM noise current $I_{CM}(s)$ on the DC side is given by

$$I_{CM}(s)=\frac{1-A(s)}{1-A(s)/(1+Z_{CM}(s)/Z_{LISNs}(s))}\cdot I_{CMO}(s) \quad (19)$$

In Eq. (19), $I_{CMO}(s)$ represents the bare CM noise current without the AEF. According to Eq. (19), to achieve a good CM EMI suppression effect, $A(s)$ should approach unity, and the amplitude of $Z_{CM}(s)$ should be much larger than that of the $Z_{LISNs}(s)$. Fig. 24

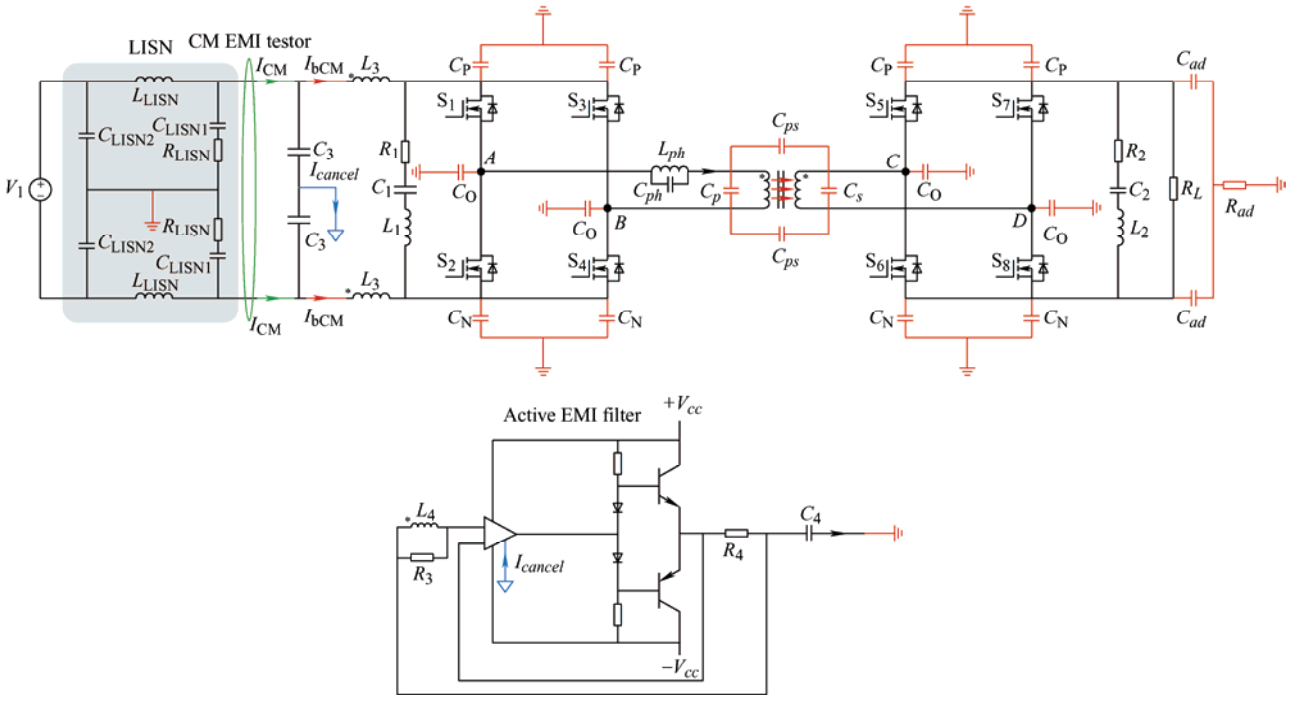

Fig. 24 Topology of the DAB with the proposed AEF

shows the detailed topology of the DAB with the proposed AEF. To make the CM loop clearer, an extra designed C_{ad} and R_{ad} are added, and the CM current flows through this circuit to the ground. In addition, the CM impedance relationship of the proposed AEF is satisfied.

The DC bus was used as the one-turn-winding primary inductor L_3 to detect the entire CM current flowing through the system. The secondary inductor L_4 was paralleled to resistor R_3 to generate a voltage drop for the AEF input. Subsequently, the compensating current I_{cancel} was produced by the amplification circuit of the AEF and injected into the DC side. An extra class AB push-pull amplification circuit was used to enhance the output ability to compensate for the current. The EMI tester was placed on the DC bus to obtain the frequency spectrum of the CM current. To ensure that $A(s)$ is unity, the winding turns of the secondary inductor were set to 10, and R_3 was 10 times that of R_4. AD826 was used as the op-amp, and FZT692B and FZT792A were used as complementary transistors in the push-pull circuit. Tab. 5 lists the component parameters.

Tab. 5 Detailed parameters of components

Components	Value	Components	Value
Turns of L_3	1	C_3/μF	2.2
Turns of L_4	10	C_4/μF	3.3
R_3/Ω	30	C_{ad}/μF	3.3
R_4/Ω	3	R_{ad}/Ω	150

Fig. 25 shows the implementation of the AEF. An inductance coil with concentric windings was used as the secondary side of the transformer. The proposed AEF senses the CM noise I_{bCM} and generates an inverse compensating current I_{cancel} to be injected forward into the DC bus. Fig. 26 was obtained when the power supply was 200 V and the switching frequency was 10 kHz. This shows a comparison between I_{bCM} and I_{cancel}. The main components of the CM current are the cardinal harmonics of switching frequency. The compensating current I_{cancel} counteracts the sensed signal I_{bCM} well in the low-frequency band. However, the compensation effect of the high-frequency burrs was limited. The CM EMI current tester was placed on the DC bus before the injection point. Fig. 27 shows the tested spectrum of the CM noise. Compared with the bare CM noise current, there was a CM reduction effect of approximately 25 dB of the CM noise with the AEF for low-frequency switching harmonics below several hundred kilohertz. The compensation effect for high-frequency noise weakened because of the parasitic parameters of the AEF and the limitation of the op-amp capacity.

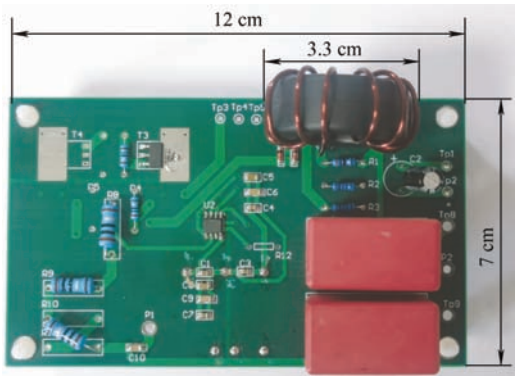

Fig. 25 The implementation board of AEF

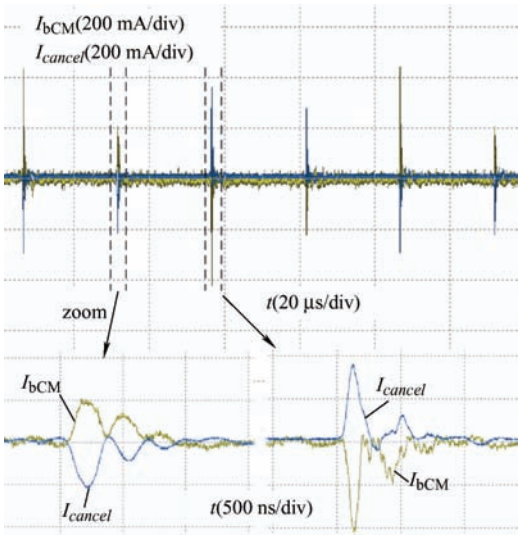

Fig. 26 Comparison of I_{bCM} and I_{cancel}

The VSF modulation disperses the energy of the narrow-band harmonic to a wider spectrum range, such that the harmonic spikes are attenuated and smoothed. In contrast to the VSF modulation, the AEF injects compensating signals to attenuate the sensed EMI. When both methods are adopted, they do not conflict in theory. An experiment using a combination of the VSF modulation and AEF was performed to test the EMI reduction effect, as shown in Fig. 28. With the combination of the proposed VSF modulation and AEF, the compensation effect within several hundred kilohertz was enhanced to 30 dB, better than 10 dB when using the VSF modulation alone. Owing to the

disadvantage of the AEF, the suppression effect for high-frequency noise was weak.

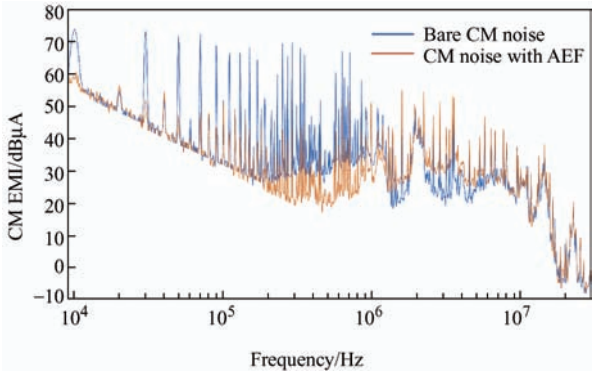

Fig. 27 Tested CM EMI with and without the proposed AEF

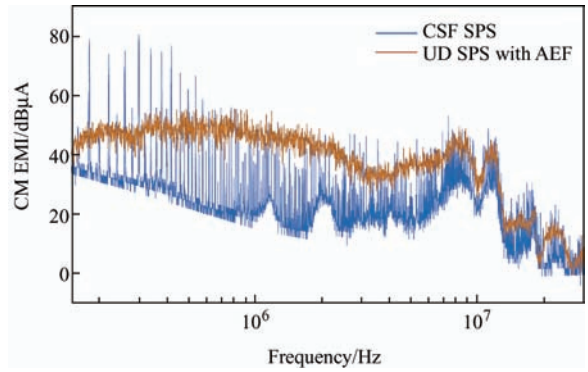

Fig. 28 Tested CM EMI reduction with VSF (UD-SPS) and the proposed AEF

5 Conclusions

This study discusses the problem of CM EMI in SSTs. Owing to the switching of primary and secondary transformers in the DAB and the parasitic parameters in the CM loop, CM EMI propagates through the SST and ground and interferes with key components in the SST. The CM EMI conductive model of SSTs was analyzed. Based on the concept of passive filtering and active mitigation, a few methods were evaluated in this study.

(1) The CM filter using the coupled inductor can be integrated with the phase-shift inductor of the DAB. Therefore, it can effectively suppress CM EMI without affecting the DAB power transmission. However, compared with the proposed VSF modulation and AEF, this method relies on SPS modulation.

(2) Periodic variation in the switching frequency can help reduce the CM EMI peak in the frequency domain. UDPWM was developed and tested in the DAB. It achieved a reduction of approximately 10 dB in the region below 1 MHz. Furthermore, this method can be extended to other modulation methods. Compared with passive filters and AEFs, there is no need to consider the complex parasitic parameters of the interference path.

(3) The AEF can sample and compensate for the CM EMI in the DAB and mitigate the CM EMI primarily below the MHz region. Compared with the other two methods, the AEF requires additional devices. However, it is universal for a variety of power electronic converters. Furthermore, the AEF can be combined with the aforementioned methods to suppress CM EMI.

With further studies, the comprehensive application of these methods can achieve better CM EMI mitigation results in SSTs.

References

[1] J E Huber, J W Kolar. Solid-state transformers: On the origins and evolution of key concepts. *IEEE Industrial Electronics Magazine*, 2016, 10(3): 19-28.

[2] B Zhao, Q Song, W Liu, et al. Overview of dual-active-bridge isolated bidirectional DC-DC converter for high-frequency-link power-conversion system. *IEEE Transactions on Power Electronics*, 2014, 29(8): 4091-4106.

[3] X She, A Q Huang, R Burgos. Review of solid-state transformer technologies and their application in power distribution systems. *IEEE Journal of Emerging and Selected Topics in Power Electronics*, 2013, 1(3): 186-198.

[4] X She, X Yu, F Wang, et al. Design and demonstration of a 3.6-kV-120-V/10-kVA solid-state transformer for smart grid application. *IEEE Transactions on Power Electronics*, 2014, 29(8): 3982-3996.

[5] M Leibl, G Ortiz, J W Kolar. Design and experimental analysis of a medium-frequency transformer for solid-state transformer applications. *IEEE Journal of Emerging and Selected Topics in Power Electronics*, 2017, 5(1): 110-123.

[6] R T Naayagi. Electromagnetic compatibility issues of dual active bridge DC-DC converter. *2013 International Conference on Energy Efficient Technologies for Sustainability*, Nagercoil, India. IEEE, 2013: 699-703.

[7] B Dwiza, J Kalaiselvi. Analytical approach for common mode EMI noise analysis in dual active bridge converter. *IECON 2020 The 46th Annual Conference of the IEEE Industrial Electronics Society*, Singapore. IEEE, 2020: 1279-1284.

[8] S Kumar, B Akin, G Gohil. EMI performance of active neutral point clamped phase leg for dual active bridge DC-DC converter. *IEEE Transactions on Industry Applications*, 2021, 57(6): 6093-6104.

[9] S Kumar, S K Voruganti, G Gohil. Common-mode current analysis and cancellation technique for dual active bridge converter based DC system. *2019 IEEE Energy Conversion Congress and Exposition (ECCE)*, 2019, Baltimore, MD, USA. IEEE, 2019: 6949-6956.

[10] T Guillod, F Krismer, J W Kolar. Electrical shielding of MV/MF transformers subjected to high dv/dt PWM voltages. *2017 IEEE Applied Power Electronics Conference and Exposition (APEC)*, Tampa, FL, USA. IEEE, 2017: 2502-2510.

[11] Z Qin, Z Shen, F Blaabjerg, et al. Modelling, analysis and mitigation of the transformer current ringing in dual active bridge converters. *2018 IEEE Energy Conversion Congress and Exposition (ECCE)*, Portland, OR, USA. IEEE, 2018: 650-655.

[12] J E Huber, J W Kolar. Common-mode currents in multi-cell solid-state transformers. *2014 International Power Electronics Conference (IPEC-Hiroshima 2014-ECCE ASIA)*, Hiroshima, Japan. IEEE, 2014: 766-773.

[13] D Jiang, J Chen, Z Shen. Common mode EMI reduction through PWM methods for three-phase motor controller. *CES Transactions on Electrical Machines and Systems*, 2019, 3(2): 133-142.

[14] J Kang, X Zhu, L Yun. Application of random PWM technology in DAB converter. *2018 IEEE International Power Electronics and Application Conference and Exposition (PEAC)*, Shenzhen, China. IEEE, 2018: 1-6.

[15] H P Park, S Jeong, M Kim, et al. Spread spectrum technique for decreasing EM noise in high-frequency APWM HB resonant converter with reduced EMI filter size. *IEEE Transactions on Power Electronics*, 2019, 34(11): 10845-10855.

[16] M Kim, H P Park, J H Jung. Spread spectrum technique with random-linear modulation for EMI mitigation and audible noise elimination in IH appliances. *IEEE Transactions on Industrial Electronics*, 2022, 69(8): 8589-8593.

[17] J Chen, D Jiang, Z Shen, et al. Uniform distribution pulsewidth modulation strategy for three-phase converters to reduce conducted EMI and switching loss. *IEEE Transactions on Industrial Electronics*, 2020, 67(8): 6215-6226.

[18] Q Li, J Chen, D Jiang. Periodic variation in the effect of switching frequency on the harmonics of power electronic converters. *Chinese Journal of Electrical Engineering*, 2020, 6(3): 35-45.

[19] Y C Son, S K Sul. A new active common-mode EMI filter for PWM inverter. *IEEE Transactions on Power Electronics*, 2003, 18(6): 1309-1314.

[20] S Wang, Y Y Maillet, F Wang, et al. Investigation of hybrid EMI filters for common-mode EMI suppression in a motor drive system. *IEEE Transactions on Power Electronics*, 2010, 25(4): 1034-1045.

[21] Y Zhang, Q Li, D Jiang. A motor CM impedance based transformerless active EMI filter for DC-side common-mode EMI suppression in motor drive system. *IEEE Transactions on Power Electronics*, 2020, 35(10): 10238-10248.

[22] C Liu, L Qi, X Cui, et al. Experimental extraction of parasitic capacitances for high-frequency transformers. *IEEE Transactions on Power Electronics*, 2017, 32(6): 4157-4167.

[23] Z Qin, Z Shen, F Blaabjerg. Modelling and analysis of the transformer current resonance in dual active bridge converters. *2017 IEEE Energy Conversion Congress and Exposition (ECCE)*, Cincinnati, OH, USA. IEEE, 2017: 4520-4524.

Dong Jiang received the B.S. and M.S. degrees in Electrical Engineering from Tsinghua University, Beijing, China, in 2005 and 2007, respectively. He started working toward Ph.D. degree with the Center for Power Electronics Systems (CPES), Virginia Tech, Blacksburg, VA, USA, in 2007, and was transferred with his advisor in 2010, to the University of Tennessee, Knoxville, TN, USA, where he received the Ph.D. degree in Power Electronics and Motor Drives in 2011. He was with the United Technologies Research Center (UTRC), East Hartford, CT, USA, as a Senior Research Scientist/Engineer, from January 2012 to July 2015. He has been with the Huazhong University of Science and

Technology (HUST), Wuhan, China, as a Professor, since July 2015. His main research interests include power electronics and motor drives, with more than 100 published IEEE journal and conference papers in this area. Dr. Jiang was the recipient of six best paper awards in IEEE conferences. He is an Associate Editor for the IEEE Transactions on Industry Applications.

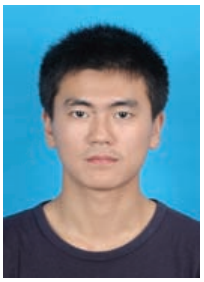

Zhenyu Wang was born in Zhejiang, China, in 1996. He has received the master's degree in Huazhong University of Science and Technology, Wuhan, China, in 2022, and he is currently working toward the Ph.D. degree in Huazhong University of Science and Technology. His main research directions are electromagnetic compatibility and AC motor drive.

Wenjie Chen received the B.S., M.S., and Ph.D. degrees in Electrical Engineering from Xi'an Jiaotong University, Xi'an, China, in 1996, 2002, and 2006, respectively.

Since 2002, she has been a member of the School of Electrical Engineering, Xi'an Jiaotong University, where she is currently a Professor. From January 2012 to 2013, she was with the Department of Electrical Engineering and Computer Science, University of Tennessee, Knoxville, TN, USA, as a Visiting Scholar. She then came back to Xi'an Jiaotong University and was engaged in the teaching and research works in power electronics. Her main research interests include electromagnetic interference, active filters, and power electronic integration.

Jianrui Liu was born in Shanxi, China, in 1999. He received the B.S. degree in Electrical Engineering in 2021 from the Huazhong University of Science and Technology, Wuhan, China, where he is currently working toward the M.S. degree in Electrical Engineering in the School of Electronic and Electrical Engineering.

His current research interests include electromagnetic interference, active EMI filtering, and electromagnetic compatibility.

Xuan Zhao received the B.S. and M.S. degrees in Electrical Engineering from Huazhong University of Science and Technology, Wuhan, China, in 2017 and 2020, respectively. He currently working toward the Ph.D. degree in Electrical Engineering with the Huazhong University of Science and Technology, Wuhan, China. His research interests include multilevel converters, AC motor drive and electromagnetic interference of power electronics system.

Wei Sun received the B.S. degree in Electrical Engineering from Beijing Jiaotong University, Beijing, China, in 2009, and the M.S. and Ph.D. in Electrical Engineering from Harbin Institute of Technology, Harbin, in 2012 and 2016 respectively. He has been with the Huazhong University of Science and Technology, Wuhan, China, as a Lecture, since November 2017. His main fields of interest are AC motor drive, control theory application in power electronics system.